PAPER

Check for updates

Laser-induced plasma on the boundary of two matrices†

Megha Mohan, [ID] *[a] Jakub Buday,[ab] David Prochazka, [ID] [ab] Pavel Gejdoš, [ID] [a] Pavel Pořízka [ID] [abc] and Jozef Kaiser [ID] [abc]

In recent years, Laser-Induced Breakdown Spectroscopy (LIBS) has gained attention as a powerful technique for the elemental imaging of samples. With increasing spatial resolution and sensitivity, new challenges arise when analyzing heterogeneous samples with multiple matrices. Specifically, there is a risk of ablation at the boundary of matrices, leading to the misinterpretation of elemental maps. In this study, we investigated the behavior of plasma plumes generated on the boundary of two well-defined matrices using a combination of three-dimensional plasma imaging, spectroscopy, and Mach–Zehnder interferometry. We examined how variations in the collection optic angles with respect to the straight line defining the boundary affect the elemental distribution in plasma plumes. Consequently, the corresponding changes in signal intensities were analyzed. We also investigated the effects of slight misalignment of the optics on the measured signals. Additionally, we used Mach–Zehnder interferometry to determine the changes in electron density and to identify any changes in the plasma plume size and shape during boundary ablation. Overall, our findings provide valuable insights into the behavior of plasma plumes at the boundary of matrices and factors that need to be considered when mapping fine heterogeneous structures using LIBS.

Introduction

Laser-Induced Breakdown Spectroscopy (LIBS) has emerged as a prominent analytical tool of choice among scientists and researchers owing to its remarkable analytical capabilities. LIBS offers the ability to analyze samples in any state of matter without any or minimal pre-treatment, coupled with real-time, rapid, and simultaneous detection of almost all elements in the periodic table.[1,2] Another unique feature of LIBS is the capability of stand-off measurements[3,4] making it an invaluable tool for a diverse range of applications ranging from environmental monitoring,[5,6] detection of explosives[7] and hazardous materials[8] to extra-terrestrial exploration.[9–11] One of the most significant advantages of LIBS is the ability of very fast and responsive spatially resolved multi-elemental imaging of samples. It is a potential application of LIBS, which has seen significant developments in instrumentation and applications in recent years.[12]

While the overall elemental composition of materials is often sufficient for analysis in some cases, in many applications, a more detailed elemental distribution within the sample is necessary. In such situations, LIBS-based elemental imaging has proven to be a promising technique in the range of spatially resolved analysis methods.[13] In LIBS-based imaging, a pre-defined laser sequence is employed to generate a series of laser-induced plasma at various positions on the sample surface, effectively covering the region of interest. The radiation emitted by the plasma plume is captured using a spectrometer, and the elemental signal or information is extracted from the emission spectra. Thus, elemental maps can be obtained in a pixel-by-pixel manner.[14] LIBS-based imaging offers unique features in comparison to the conventional elemental imaging methods such as Laser Ablation Inductively Coupled Plasma Mass Spectrometry (LA-ICP-MS),[15,16] micro-X-ray Fluorescence (μ-XRF),[17,18] X-ray Photoelectron Spectroscopy (XPS),[19] Secondary Ion Mass Spectrometry (SIMS),[20] Auger Electron Spectroscopy (AES),[21] *etc.* The key benefit of using LIBS for elemental imaging is its unique combination of speed, sensitivity, and spatial resolution, irrespective of the sample size. A single laser pulse can ablate and vaporize a small region of the sample, generating the plasma plume. This simplicity provides several advantages, such as an all-optical design compatible with conventional microscopy, fast operating speed up to kHz, and the ability to operate in an ambient atmosphere.[14] Another feature of LIBS-based imaging is that it provides elemental maps with a microscopic resolution.[13] Furthermore, LIBS enables simultaneous multi-element detection with detection

[a]Central European Institute of Technology, Brno University of Technology, Purkyňova 656/123, Brno, Czech Republic. E-mail: mohanm@vutbr.cz

[b]Faculty of Mechanical Engineering, Brno University of Technology, Technická 2, Brno, Czech Republic

[c]Lightigo s.r.o., Brno-venkov, Hlavní 104, 664 31 Lelekovice, Czech Republic

This journal is © The Royal Society of Chemistry 2023

J. Anal. At. Spectrom., 2023, **38**, 2433–2440 | **2433**

limits in the range of ppm for most of the elements with no constraints for the detection of light elements.[12] Additionally, quantitative analysis is possible using standards with known concentrations.[22,23] The possibility of achieving microscopic resolution with a ppm-scale sensitivity while ensuring a fast acquisition rate up to 1 kHz has expanded the potential applications of LIBS-based mapping in various fields.[24–26] LIBS has repeatedly demonstrated its bioimaging applicability in imaging plant samples,[27,28] Tag-LIBS,[29] and in tracing the uptake, distribution, and bioaccumulation of elements in organisms, organs, and diseased tissues.[30–32] In addition to its compelling applications in life sciences, LIBS-based imaging is also widely used in geoscientific studies,[33,34] material science,[35] cultural heritage studies,[36] and many other fields that require spatially resolved analysis.

Despite its potential to provide a detailed elemental distribution of samples, LIBS-based mapping is not without its limitations. It is limited by the trade-off between spatial resolution and sensitivity. The spatial resolution of LIBS systems is controlled by the spot size of the laser beam, with a high spatial resolution for small spot sizes. However, smaller spots result in reduced sensitivity due to the decreased ablated mass. Another major limitation is while dealing with highly heterogeneous samples that have complex matrices. LIBS-based imaging can effectively analyze various materials, including homogeneous matrices with minor or trace elements. Such materials offer the advantage of avoiding so-called matrix effects, simplifying the calibration of raw intensities.[14] However, this is not the case while dealing with heterogeneous samples. For instance, these samples contain a mixture of two or more different matrices that are not evenly distributed throughout the sample. Smaller laser spots allow the ablation of a higher percentage of total area, and the chance of ablating a boundary between two or more matrices increases. The boundary of two materials in a heterogeneous sample can be a complex region with unique properties, unlike the other regions in the sample. Therefore, ablating the boundary results in biased signal intensities and uncertainty in chemical mapping, which also significantly affect the quantitative results. Thus, it is essential to study the plasma plume during the ablation of multiple matrices at once in the mapping of heterogeneous samples so that the uncertainties in the chemical mapping could be reduced. Integrating plasma visualization techniques, such as direct imaging, shadowgraphy, interferometry, etc., with LIBS spectra offers a viable pathway to enhance measurement accuracy, providing valuable insights into plasma plume morphology and dynamics.[37–39] The spectra on the boundary of two well-defined matrices were previously studied by Holub et al. using chemometric algorithms.[40] However, this study was limited to the spectral response and its challenges in applying chemometric algorithms. Hai et al. studied the mixing dynamics of isolated plasmas formed at the interface between Cu and Sn–Pb samples using femtosecond laser pulses. This study analyses the spatial and temporal mixing dynamics, plasma expansion, and its characteristics emphasizing the importance of precise timing in the signal collection during LIBS imaging measurements.[41] While this study focused on femtosecond ablation and its plasma dynamics, the cause of spectral bias and uncertainty during nanosecond ablation of material boundaries remains unclear. This fundamental difference in laser pulse duration leads to distinct mechanisms of energy absorption and target ablation. For instance, in ns laser ablation, ionization, heating, and vaporization occur during the laser pulse duration itself. In contrast, fs laser ablation deposits all laser energy directly onto the target surface.[42] These contrasting ablation mechanisms have significant implications for the dynamics of the ablated material, particularly in terms of plasma plume behavior.

Therefore, the objective of this research is to investigate the behavior of plasma plumes during nanosecond laser ablation of material boundaries. This is achieved through a combination of direct plasma imaging, spectroscopy, and Mach–Zehnder interferometry to analyze the plasma plume. In this work, copper (Cu) and tin (Sn) matrices are used to define the transition boundary. Two-dimensional plasma imaging with an ICCD camera is a valuable tool for studying the plasma morphology and distribution of excited species in a laser-produced plasma system. In this study, we collected 2D plasma plume images from various angles with respect to the boundary to analyze the distribution of Cu and Sn in the plasma plume using bandpass filters. The impact of these changes on the relative intensity of spectral lines is analyzed together with the effect of misaligned collection optics on the spectral signal. Furthermore, Mach–Zehnder interferometry is utilized to analyze the variation of electron density, size, and shape of the plasma plume.

Materials and methods

Samples

In this work, the focus is to study the boundary between Cu and Sn metals. The boundary of Cu and Sn is interesting due to their different physical properties, chemical behavior, and most importantly, their potential industrial applications in the form of a wide range of alloys. For preparing the sample, unalloyed Cu (CW004A) and Sn (Sn70Zn) which contains 70% Sn, and the rest of the material Zn, was used. The samples were joined by embedding them in epoxy resin, which ensured a proper adhesion and alignment, resulting in a well-defined boundary for ablation.

Experimental setup

Fig. 1a, shows the experimental setup used for our measurements. The ablation laser (532 nm, 25 mJ, pulse width $\approx$ 10 ns) was focused on the sample using a fused silica triplet (focal length 50 mm) to create the plasma. The spot size of the laser beam was 100 μm and the ratio of Cu and Sn irradiated areas was 50 : 50. Plasma images were acquired using an ICCD (Andor, iStar) camera after passing through bandpass filters with central wavelengths around 510 nm and 380 nm (with a full width half maximum of 10 nm) to acquire the images corresponding to the distribution of Cu and Sn respectively. Radiation of the plasma was also collected using a collimator (38.5 mm focal length) and optical fiber with a 400 μm core diameter onto an echelle spectrometer (resolution of $\lambda/\Delta\lambda$ up to 5000) equipped with an ICCD camera while the focus of the collection optics remained centered relative to the plasma plume.
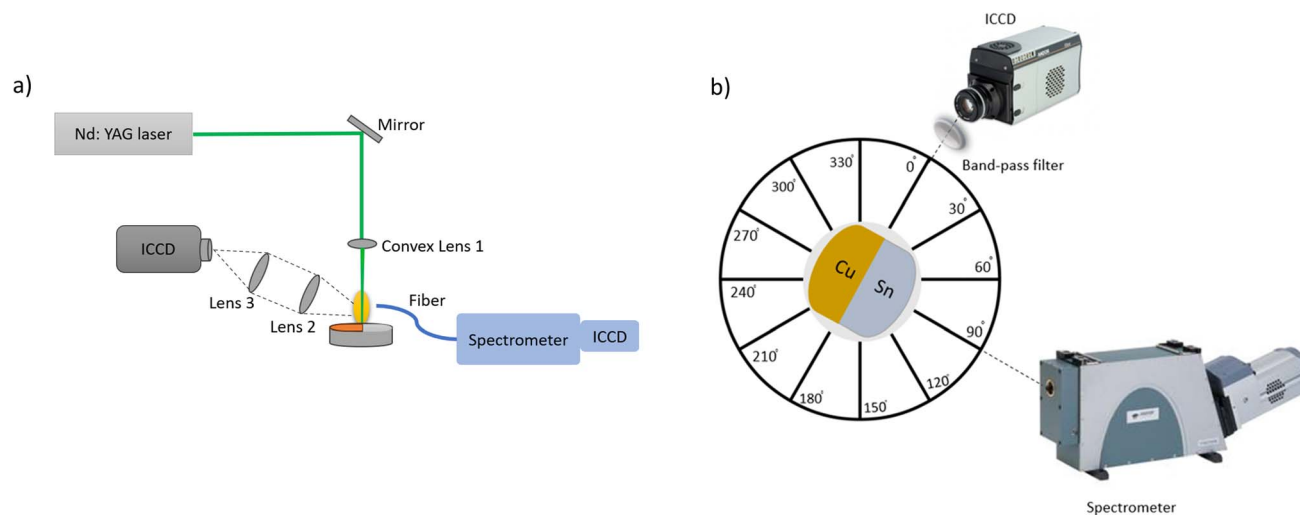
2434 | J. Anal. At. Spectrom., 2023, 38, 2433–2440

This journal is © The Royal Society of Chemistry 2023

Fig. 1 (a) Experimental set-up for simultaneous collection of spectra and plasma images on the Cu and Sn matrix boundary. (b) Top view illustrating the precise angles of collection for data acquisition.

The laser was directed perpendicular to the surface of the sample during the ablation process. As shown in Fig. 1b., the plasma images and spectra were collected from two different angles. However, this does not pose a limitation as we rotated the sample in the range of 0–360° with a step size of 30°. This ensured that the spectra corresponded to the image collected from another angle. 0° means that the boundary is collinear to the imaging axis with Cu on the right and Sn on the left side with respect to the ICCD camera. The other angles are the respective shifts of the boundary with respect to the imaging axis. For each angle, we captured the plasma plume images using bandpass filters centered at 510 nm and 380 nm separately. The filters were specifically chosen to correspond to the Cu I 510.55 nm and Sn I 380.10 nm spectral lines. By selectively capturing the light emitted from the elements using the filters, we were able to eliminate any interference from other light sources and study the distribution of the elements of interest.

For Mach–Zehnder interferometry measurements, a continuous laser with a wavelength of 532 nm was used as a probe beam. The probe beam was split into two optical paths (reference and object path), recombined with a beam splitter, and then captured using the ICCD camera that was used for the direct imaging experiments.

Measurement parameters

An ablation laser with a wavelength of 532 nm and pulse energy of 25 mJ was used to create the ablation on the sample. The ICCD camera was set to acquire the plasma images 1.5 μs after laser ablation and the duration of exposure was 100 ns with a Micro-Channel Plate (MCP) gain of 40. Spectra were collected simultaneously using an echelle spectrometer equipped with an ICCD camera 1.5 μs after ablation with a gate width of 100 ns and an MCP gain of 180. The sample was rotated from 0° to 360° with a step size of 30°, and for each angle, 20 repetitions were performed. The possibility of back deposition of the material is avoided in our case because each time the ablation was on a fresh spot on the boundary.

Results

Plasma homogeneity on heterogeneous sample boundary

We investigated the influence of the angle of collection optics relative to the boundary on the elemental distribution in plasma plume generated at the boundary of Cu and Sn. To selectively study the distribution of Cu and Sn in the plasma, we employed time-gated imaging using bandpass filters. Separate plasma images corresponding to the distribution of Cu and Sn were acquired and then combined to produce the images presented in Fig. 2. In the figure, 0° means that the boundary is collinear to the imaging axis with Cu on the right and Sn on the left side with respect to the ICCD camera. In this combined image, Cu is shown in red, Sn in green, and the areas where the two elements overlap are partially yellow. For each angle, a total of 20 images were collected, and the images shown in Fig. 2 represent the average of those 20 images. Our results demonstrate that the plasma is inhomogeneous and the elements in plasma tend to be more dominant on the respective sides facing the ICCD camera while rotating the sample.

Our results show that the location and distribution of elements in the plasma plume are influenced by the orientation of the sample relative to the imaging camera. Specifically, when Cu is on the right side of the sample with respect to the camera, the distribution of Cu in the plasma plume is more dominant on the right side of the ICCD image. As the sample is rotated clockwise, the distribution of Cu becomes more symmetrical between angles of 90° and 150°. However, for angles between 180° and 240°, the distribution of Cu becomes more dominant on the left side of the ICCD image before returning to the initial state between angles of 270° and 330°. In contrast, Sn tends to concentrate in the middle and top regions of the plasma plume compared to Cu. This behavior can be attributed to the difference in melting points between Sn and Cu. When using a laser with a wavelength of 532 nm and low irradiance, the plasma is considered to be in the Laser-Supported Combustion (LSC) regime. In the plasma dominated by LSC wave mode, the

This journal is © The Royal Society of Chemistry 2023

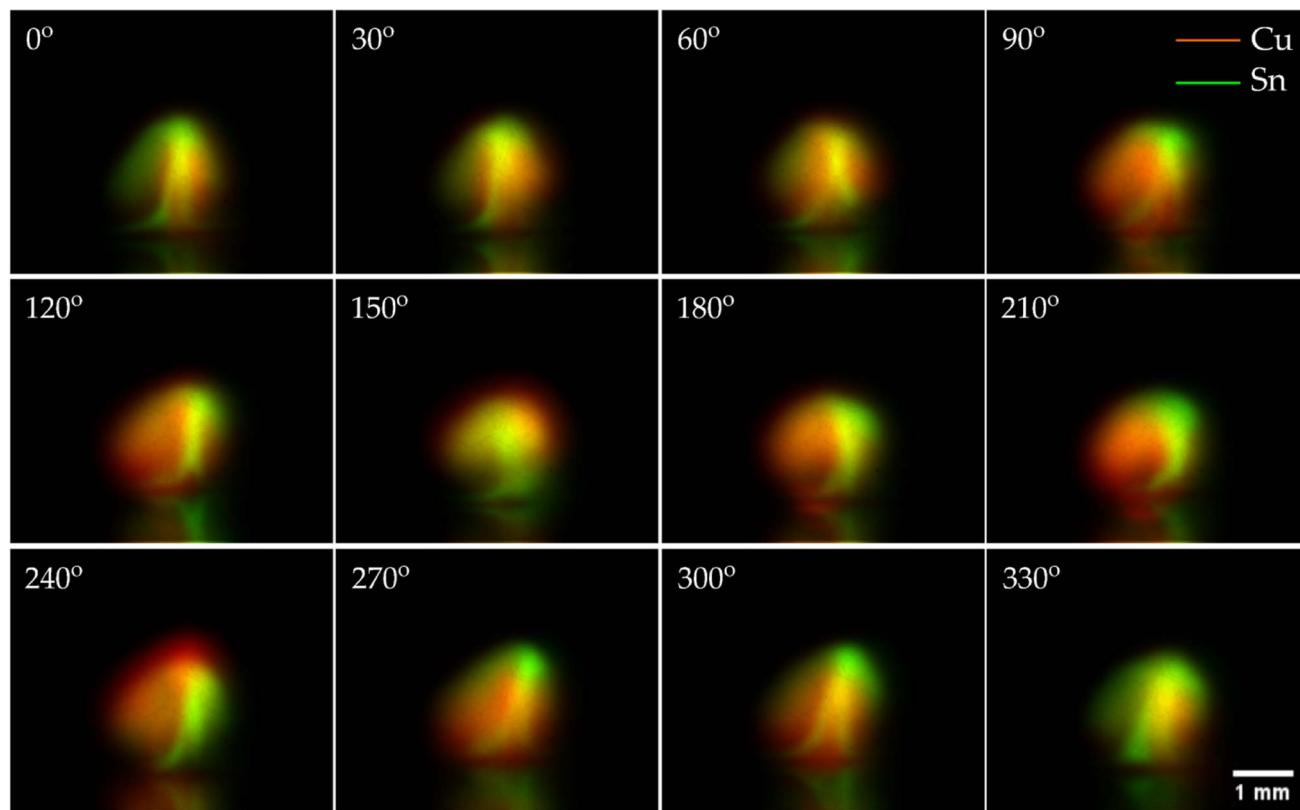*J. Anal. At. Spectrom.*, 2023, **38**, 2433–2440 | **2435**

Fig. 2   Distribution of Cu (in red) and Sn (in green) in the plasma plume, as visualized using time-gated imaging for collection angles ranging from 0° to 360°. The images were acquired at a delay of 1.5 µs after ablation with a detector gate width of 100 ns.

distribution of species is primarily influenced by the melting point of elements in the alloy, and the element with the lower melting point will be melted away first.[43] In this case, Sn melts before Cu and expands into the surrounding gas perpendicular to the sample surface. Hence, due to the mechanics of ablation, Sn is mostly populated in the middle and top portions of the plasma plume. The thermal properties of the materials also affect the dimension of ablation craters. The ablation craters in pure Cu and pure Sn under the same laser irradiance reveal a larger ablation crater in the case of Sn. Whereas at the boundary of Cu and Sn, the ablation crater exhibits a symmetric pattern. Sn showcases a deeper crater, indicating a greater ablated mass compared to Cu (see ESI†). This outcome can be attributed to the higher sensitivity of Sn to the thermal effects of the laser. As the laser energy is absorbed, the lower melting point of Sn facilitates rapid melting and ablation, leading to a more pronounced ablation crater.

These findings reveal that the plasma plume generated on the boundary of two matrices is inhomogeneous in nature and varies in elemental distribution with different collection angles.

Analysis of signal intensities as a function of angle between boundary and collection optics

Having established that the elemental distribution in plasma generated at the boundary of matrices varies with the angle of collecting the plasma images, we investigated the influence of collection angle on the signal intensities as well. To accomplish

this, spectra were collected simultaneously using an echelle spectrometer. Although the spectra were collected from a different angle, in Fig. 3, the 0-degree point refers to the position relative to the imaging camera. The data was rearranged to ensure that the 0-degree position in Fig. 2 is comparable to the 0-degree position in Fig. 3, both of which are referenced to the imaging camera.

We focused on the spectral lines that corresponded to the bandpass filters, specifically the 380.10 nm line of Sn I and the 510.55 nm line of Cu I. In the context of this study, it is important to emphasize that the specific ablated masses of the materials do not play a significant role in the interpretation of the results. Ablated mass influences the number of analyte atoms available for excitation, which, in turn, affects the population of excited states and, consequently, the intensity of the spectral lines. To address this, we performed separate univariate normalization for the lines before comparing the intensities shown in Fig. 3. Here, it can be observed that the Cu signal increases and reaches its maximum at 90°, before decreasing to a minimum at 270°. This behavior may be attributed to the partial dependence of the position of elements on the boundary relative to the camera, as we saw in the direct imaging section of this manuscript. The experimental results demonstrate a different pattern for Sn in comparison to Cu. One of the possible explanations for this disparity lies in the symmetrical distribution of Sn within the plasma plume compared to Cu, as discussed in the initial section of the results. As a result, even
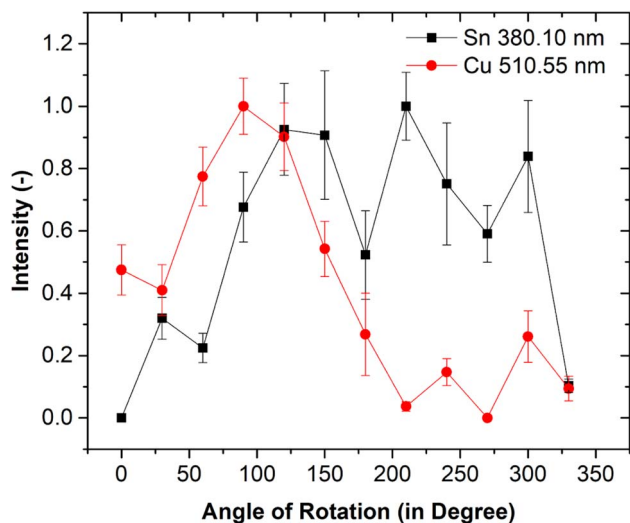
Fig. 3 Dependence of the intensities of Cu and Sn spectral lines on the angle of collection for the plasma radiation. Spectra were acquired 1.5 μs after the ablation, with a gate width of 100 ns, which is the same acquisition condition as for plasma images.

with the rotating collection optics, a considerable portion of the middle and top regions of the plume, where Sn is predominantly concentrated, is captured, resulting in relatively lower fluctuation of Sn compared to Cu. Furthermore, the optical properties of the plume may also contribute to these observations.

In order to quantify the fluctuation of intensities while ablating the boundary of matrices, the intensities of pure Cu and Sn were measured. The relative standard deviation (RSD) of Cu 510.55 nm and Sn 380.10 nm lines in the pure samples were found to be less than 10% and 15%, respectively (see ESI†). These RSD values represent the average fluctuations across all measured angles. These values indicate that the intensity fluctuations for both elements are minimal and that the intensities of Cu 510.55 nm and Sn 380.10 nm remained nearly constant regardless of the angle of the collection optics when measured on pure samples. This behavior can be attributed to the homogeneity of the matrices, which leads to symmetric distribution in the plasma plume. However, we observed an increase in the RSD of approximately 40% and 24% for Cu and Sn lines, respectively, at the boundary. These higher RSD values at the matrix boundary indicate that there are distinct variations in the signal intensities on the boundary of the two matrices.

Impact of misaligned collection optics on signal intensity

Although it is a common practice to ensure centered collection of the spectrometer with respect to the plasma plume prior to measurements, in this section we investigate the impact of even a slight deviation in alignment on the resulting spectra. We shifted the collection optics from the centered position by 382 μm and 764 μm in the same direction as shown in Fig. 4. The study was performed to emphasize the importance of accurate alignment in obtaining reliable results. Fig. 5 shows the observed deviations in the intensities for the shifts with respect

to the plasma plume position for Cu I 510.55 nm and Sn I 380.10 nm spectral lines.

To quantify the impact of the shifted optics on the intensity of spectral lines, we have compared the intensity ratio of 510.55 nm Cu I and 380.10 nm Sn I line of centered collection to the 382 μm and 764 μm shifts. The results are shown in Fig. 6a and b corresponding to Cu and Sn lines, respectively.

Fig. 6a and b show that, in most cases, the intensity ratio is greater than one. This indicates that the intensities of the Cu I and Sn I lines are higher for centered collection optics. Additionally, the intensity decrease is more pronounced for a 764 μm shifted position, indicating that the displacement from the central collection point has a greater impact on the intensity of the spectral lines.

Analyzing the plasma properties using Mach–Zehnder interferometry

Since the matrices differ not only in the chemical composition but also in the physical and mechanical properties, we analyzed the plasma using Mach–Zehnder interferometry to analyze changes in the free electron density. Mach–Zehnder interferometry is a non-intrusive diagnostic technique in which the relative phase shift between two collimated beams is used to calculate the free electron density in the plasma plume as well as to visualize the plasma plume in terms of its size and shape.[44,45] The interferometry method utilizes the fact that the plasma index of refraction is proportional to the free electron density in plasmas. The variation in the index of refraction is similar to a change in the path length of the probe laser beam, resulting in a phase shift, which can be determined by the fringe amplitude of the combined probe and reference beams. As the elemental distribution varied with collection angles, it was of interest to investigate whether these changes would be reflected in electron density.

In Fig. 7a, we present the interferometric image obtained at 180° of rotation. Our analysis of the image revealed that, despite the clear separation of Cu and Sn observed in the plasma (Fig. 7b), there was no spatial discontinuity of electron density in the plasma. The average electron density for the images captured at 1.5 μs after ablation for all the collections was
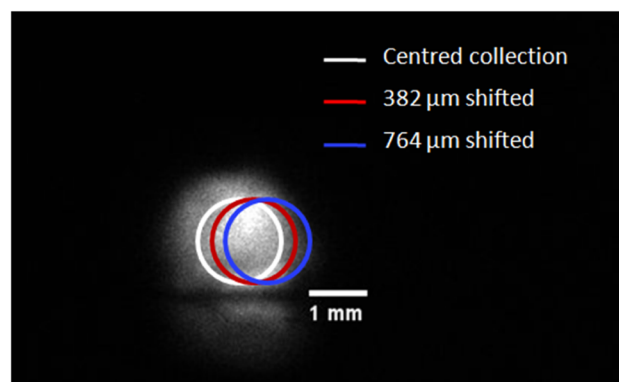

Fig. 4 Illustration of the shifts in position of collecting the plasma radiation with respect to the ICCD acquired image of the plasma.

This journal is © The Royal Society of Chemistry 2023

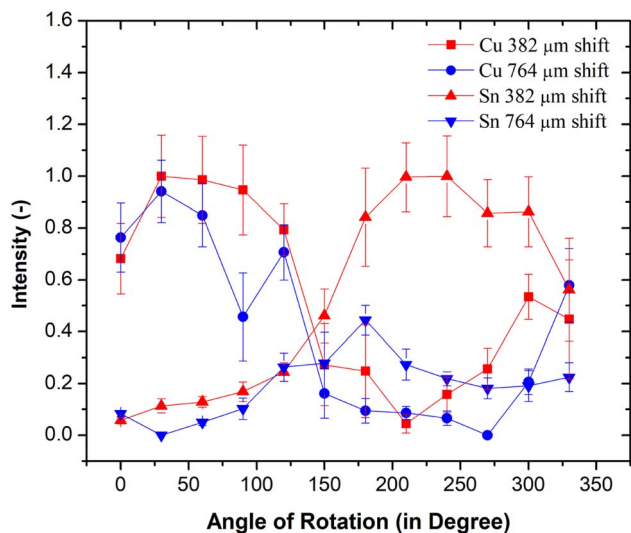*J. Anal. At. Spectrom.*, 2023, **38**, 2433–2440 | **2437**

Fig. 5 Deviation in signal intensities of Cu I 510.55 nm line and Sn I 380.10 nm line for the respective shifts in the position of collection optics.

calculated to be in the range from 1.4×10^{17} to 4.2×10^{17} electrons per cm³ of plasma. The Stark broadening method was used as the reference method for Mach–Zehnder interferometry. Cu I 510.55 nm line was used to calculate the electron number density, and the same procedure as mentioned in the references was followed[46,47] (see ESI†). The average electron number densities obtained from the Stark broadening method could be compared with the results from Mach–Zehnder interferometry with the average electron densities in the order of 0.3×10^{17} to 2.1×10^{17} electrons per cm³ and 1.4×10^{17} to 4.2×10^{17} electrons per cm³ of the plasma plume respectively.

Discussion

In the presented work, we studied the properties of the plasma plume generated at the boundary of two matrices, Cu and Sn, using a combination of time-gated imaging, spectroscopy, and interferometry. Our results from the direct imaging of the plasma show that the elemental distribution within the plasma is not uniform and varies with different angles of collection relative to the boundary, suggesting that the plasma plume is inhomogeneous in nature for heterogeneous samples. Even though we observed a clear separation of Cu and Sn at certain angles of rotation, at other angles, the two elements were mostly mixed together. With the improving resolution of LIBS elemental imaging, there is a greater chance of ablating the boundary between multiple matrices in a heterogeneous sample. Therefore, it is important to account for the inhomogeneous nature of the plasma plume while interpreting the results.

While plasma imaging is primarily used for visualization, elemental imaging using LIBS relies on the intensities of spectral lines to identify and quantify elements in a sample. Therefore, we studied the signal intensities as a function of different angles of collection and observed fluctuations in the intensities with varying angles of collecting the plasma radiation. Our initial assumption was that there would be little difference in signal intensities because the radiation should easily pass through the plasma plume. The signal intensities of Cu I 510.55 nm and Sn I 380.10 nm were examined, and it was found that the intensity fluctuated as a function of the angle of rotation. A higher absolute intensity of Sn compared to Cu could be due to a higher transition probability of 380.10 nm line of Sn I compared to the Cu I 510.55 nm line and the higher ablated mass of Sn compared to Cu.

To identify the potential sources of error in measurements and to understand the importance of centered alignment of the collection optics, the signal intensity studies performed with the collection optics shifted by a few micrometers. The results, illustrated in Fig. 5 and 6, reveal a noticeable deviation in signal intensity caused by the misalignment of the optics with a higher intensity for centered collection optics.

Mach–Zehnder interferometry was employed to analyze the properties of the plasma plume generated at the boundary of Cu and Sn. Our analysis showed that despite changes in elemental distribution with collection angles, there was no spatial
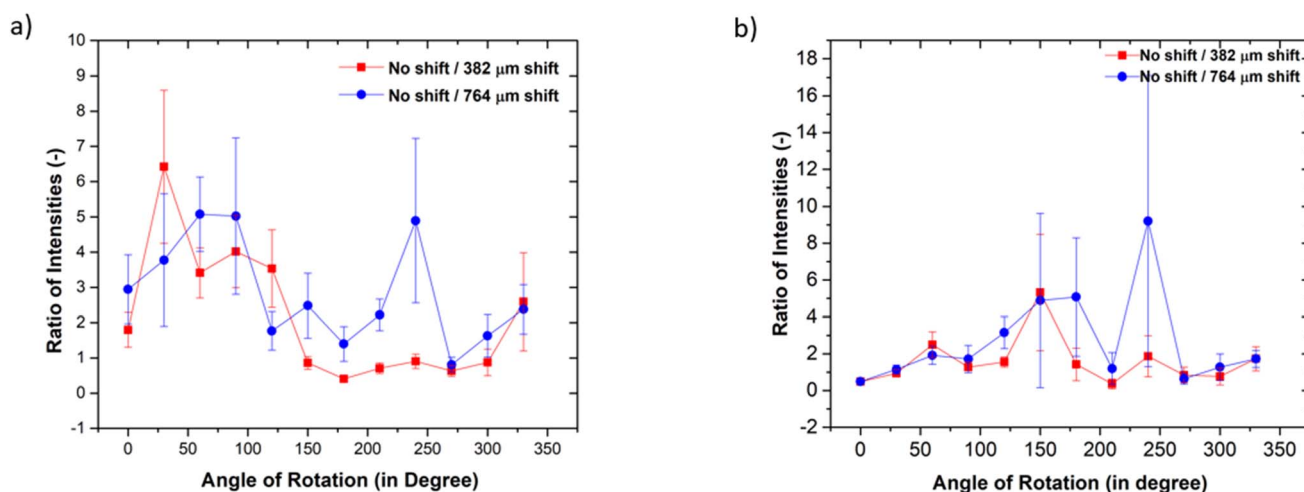

Fig. 6 The ratio of intensities for the centered collection optics to the shifted collection for (a) Sn I 380.10 nm (b) Cu I 510.55 nm spectral lines.
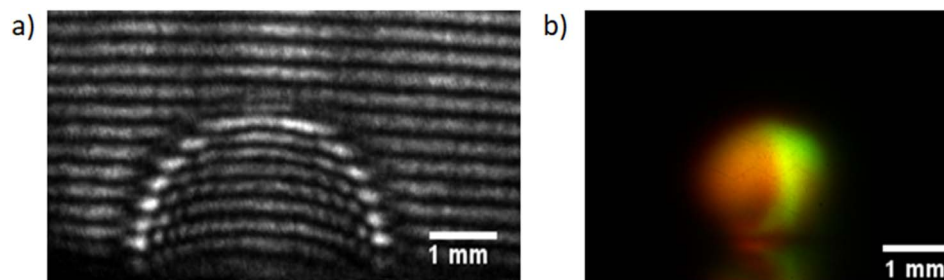
2438 | *J. Anal. At. Spectrom.*, 2023, **38**, 2433–2440

This journal is © The Royal Society of Chemistry 2023

Fig. 7 (a) Interferometry image for 180° of rotation of the boundary with respect to the camera. The image was acquired at 1.5 μs after ablation with exposure duration of 100 ns (b) distribution of elements in the plasma for 180° rotation of the boundary with respect to the camera.

discontinuity in the electron density in the plasma. The average order of the electron density remains the same and was calculated to be in the order 10^{17} electrons per cm^3 of plasma. No distortion in the size or shape of the plasma was observed. These findings suggest that the elemental distribution observed in the plasma plume is not strongly correlated with the electron density.

Conclusion

In conclusion, our study provides valuable insights into the properties of plasma generated at the boundary of Cu and Sn matrices using techniques such as time-gate imaging, spectroscopy, and interferometry. Our observations of the non-uniform elemental distribution within the plasma with varying angles of collection optics highlights the need to consider the inhomogeneous nature of plasma during the elemental imaging of heterogeneous sample. Also, this inhomogeneity is correlated to the sample or boundary orientation with respect to the optical axis of the camera. We found fluctuations in the signal intensities of Cu and Sn with varying angles of collection and identified the importance of centered alignment of collection optics in reducing sources of error in measurements. The interferometry analysis showed no significant difference in the average electron density or size and shape of plasma despite the changes in elemental distribution with collection angles. Thus, our findings provide an understanding of the morphology and behavior of plasma generated on the boundary of two matrices and highlight the important factors to be considered while mapping fine heterogeneous structures using LIBS to avoid misinterpretation of elemental maps.

Conflicts of interest

The authors declare no competing interests.

Acknowledgements

References

1 D. A. Cremers and L. J. Radziemski, *Handbook of Laser-Induced Breakdown Spectroscopy*, John Wiley & Sons, Ltd, Chichester, UK, 2006.

2 D. W. Hahn and N. Omenetto, *Appl. Spectrosc.*, 2010, 335A–366A.

3 K. Y. Yamamoto, D. A. Cremers, M. J. Ferris and L. E. Foster, *Appl. Spectrosc.*, 1996, **50**, 222–233.

4 R. T. Wainner, R. S. Harmon, A. W. Miziolek, K. L. McNesby and P. D. French, *Spectrochim. Acta, Part B*, 2001, **56**, 777–793.

5 R. S. Harmon, F. C. De Lucia, A. W. Miziolek, K. L. McNesby, R. A. Walters and P. D. French, *Geochem.: Explor., Environ., Anal.*, 2005, **5**, 21–28.

6 B. Bousquet, G. Travaillé, A. Ismael, L. Canioni, K. Michel-Le Pierrès, E. Brasseur, S. Roy, I. Le Hécho, M. Larregieu and S. Tellier, *Spectrochim. Acta, Part B*, 2008, **63**, 1085–1090.

7 J. L. Gottfried, F. C. De Lucia, C. A. Munson and A. W. Miziolek, *Anal. Bioanal. Chem.*, 2009, **395**, 283–300.

8 F. C. DeLucia, A. C. Samuels, R. S. Harmon, R. A. Walters, K. L. McNesby, A. LaPointe, R. J. Winkel and A. W. Miziolek, *IEEE Sens. J.*, 2005, **5**, 681–689.

9 D. W. Hahn and N. Omenetto, *Appl. Spectrosc.*, 2012, 347–419.

10 F. Colao, R. Fantoni, V. Lazic, A. Paolini, F. Fabbri, G. G. Ori, L. Marinangeli and A. Baliva, *Planet. Space Sci.*, 2004, **52**, 117–123.

11 S. Musazzi and U. Perini, *Springer Series in Optical Sciences 182 Laser-Induced Breakdown Spectroscopy Theory and Applications*, 2014.

12 L. Jolivet, M. Leprince, S. Moncayo, L. Sorbier, C.-P. Lienemann and V. Motto-Ros, *Spectrochim. Acta, Part B*, 2019, **151**, 41–53.

13 A. Limbeck, L. Brunnbauer, H. Lohninger, P. Pořízka, P. Modlitbová, J. Kaiser, P. Janovszky, A. Kéri and G. Galbács, *Anal. Chim. Acta*, 2021, **1147**, 72–98.

14 V. Motto-Ros, V. Gardette, L. Sancey, M. Leprince, D. Genty, S. Roux, B. Busser and F. Pelascini, *Spectroscopy*, 2020, **35**, 34–40.

15 D. Pozebon, G. L. Scheffler, V. L. Dressler and M. A. G. Nunes, *J. Anal. At. Spectrom.*, 2014, **29**, 2204–2228.

16 J. S. Becker, M. Zoriy, A. Matusch, B. Wu, D. Salber, C. Palm and J. S. Becker, *Mass Spectrom. Rev.*, 2010, **29**, 156–175.

This journal is © The Royal Society of Chemistry 2023

J. Anal. At. Spectrom., 2023, **38**, 2433–2440 | **2439**

17 F. Colao, R. Fantoni, P. Ortiz, M. A. Vazquez, J. M. Martin, R. Ortiz and N. Idris, *Spectrochim. Acta, Part B*, 2010, 688–694.

18 C. G. Worley, S. S. Wiltshire, T. C. Miller, G. J. Havrilla and V. Majidi, *J. Forensic Sci.*, 2006, **51**, 57–63.

19 M. P. Seah, *Surf. Interface Anal.*, 1980, **2**, 222–239.

20 T. Wirtz, P. Philipp, J. N. Audinot, D. Dowsett and S. Eswara, *Nanotechnology*, 2015, **26**, 434001.

21 C. J. Powell and M. P. Seah, *J. Vac. Sci. Technol., A*, 1990, **8**, 735–763.

22 F. Trichard, L. Sorbier, S. Moncayo, Y. Blouët, C.-P. Lienemann and V. Motto-Ros, *Spectrochim. Acta, Part B*, 2017, **133**, 45–51.

23 S. Pagnotta, M. Lezzerini, B. Campanella, G. Gallello, E. Grifoni, S. Legnaioli, G. Lorenzetti, F. Poggialini, S. Raneri and A. Safi, *Spectrochim. Acta, Part B*, 2018, **146**, 9–15.

24 V. Piñon, M. P. Mateo and G. Nicolas, *Appl. Spectrosc. Rev.*, 2013, **48**, 357–383.

25 P. Lucena and J. J. Laserna, *Spectrochim. Acta, Part B*, 2001, **56**, 177–185.

26 J. Kaiser, K. Novotný, M. Z. Martin, A. Hrdlička, R. Malina, M. Hartl, V. Adam and R. Kizek, *Surf. Sci. Rep.*, 2012, **67**, 233–243.

27 P. Modlitbová, P. Pořízka and J. Kaiser, *TrAC, Trends Anal. Chem.*, 2020, **122**, 115729.

28 T. Brennecke, L. Čechová, K. Horáková, L. Šimoníková, J. Buday, D. Prochazka, P. Modlitbová, K. Novotný, A. W. Miziolek and P. Pořízka, *Spectrochim. Acta, Part B*, 2023, **205**, 106684.

29 P. Pořízka, K. Vytisková, R. Obořilová, M. Pastucha, I. Gábriš, J. C. Brandmeier, P. Modlitbová, H. H. Gorris, K. Novotný and P. Skládal, *Microchim. Acta*, 2021, **188**, 1–10.

30 K. Kiss, A. Šindelářová, L. Krbal, V. Stejskal, K. Mrázová, J. Vrábel, M. Kaška, P. Modlitbová, P. Pořízka and J. Kaiser, *J. Anal. At. Spectrom.*, 2021, **36**, 909–916.

31 L. Sancey, V. Motto-Ros, B. Busser, S. Kotb, J.-M. Benoit, A. Piednoir, F. Lux, O. Tillement, G. Panczer and J. Yu, *Sci. Rep.*, 2014, **4**, 6065.

32 M. Galiová, J. Kaiser, F. J. Fortes, K. Novotný, R. Malina, L. Prokeš, A. Hrdlička, T. Vaculovič, M. N. Fišáková and J. Svoboda, *Appl. Opt.*, 2010, **49**, C191–C199.

33 D. Prochazka, T. Zikmund, P. Pořízka, A. Břínek, J. Klus, J. Šalplachta, J. Kynický, J. Novotný and J. Kaiser, *J. Anal. At. Spectrom.*, 2018, **33**, 1993–1999.

34 P. Janovszky, K. Jancsek, D. J. Palásti, J. Kopniczky, B. Hopp, T. M. Tóth and G. Galbács, *J. Anal. At. Spectrom.*, 2021, **36**, 813–823.

35 P. Lucena, J. M. Vadillo and J. J. Laserna, *Anal. Chem.*, 1999, **71**, 4385–4391.

36 A. Giakoumaki, K. Melessanaki and D. Anglos, *Anal. Bioanal. Chem.*, 2007, **387**, 749–760.

37 J. Buday, P. Pořízka and J. Kaiser, *Spectrochim. Acta, Part B*, 2020, **168**, 105874.

38 J. Buday, P. Pořízka, M. Buchtová and J. Kaiser, *Spectrochim. Acta, Part B*, 2021, **182**, 106254.

39 J. Buday, D. Prochazka, A. Záděra, V. Kaňa, P. Pořízka and J. Kaiser, *Spectrochim. Acta, Part B*, 2022, **194**, 106476.

40 D. Holub, J. Vrábel, P. Pořízka and J. Kaiser, *Appl. Spectrosc.*, 2022, **76**, 917–925.

41 R. Hai, X. Mao, G. C.-Y. Chan, R. E. Russo, H. Ding and V. Zorba, *Spectrochim. Acta, Part B*, 2018, **148**, 92–98.

42 J. R. Freeman, S. S. Harilal, P. K. Diwakar, B. Verhoff and A. Hassanein, *Spectrochim. Acta, Part B*, 2013, **87**, 43–50.

43 Y. Zhao, L. Zhang, J. Hou, W. Ma, L. Dong, W. Yin, L. Xiao, S. Jia and J. Yu, *Spectrochim. Acta, Part B*, 2019, **158**, 105644.

44 S. S. Harilal and M. S. Tillack, *Laser Plasma Density Measurements using Interferometry*, Fusion Division Center for Energy Research, University of California, San Diego, 2004.

45 H. Zhang, J. Lu, Z. Shen and X. Ni, *Opt. Commun.*, 2009, **282**, 1720–1723.

46 N. Ahmed, R. Ahmed, M. Rafiqe and M. A. Baig, *Laser Part. Beams*, 2017, **35**, 1–9.

47 R. Konjevic and N. Konjević, *Fizika*, 1986, **18**, 327–335.

2440 | *J. Anal. At. Spectrom.*, 2023, **38**, 2433–2440

This journal is © The Royal Society of Chemistry 2023